Research Article

Aqueous Cellulose Nanocrystal-Colloidal Au Inks for 2D Printed Photothermia

Marta García-Castrillo, Javier Reguera, and Erlantz Lizundia*

Cite This: ACS Sustainable Chem. Eng. 2024, 12, 1468−1479

Read Online

| ACCESS | Metrics & More | Article Recommendations | Supporting Information |

ABSTRACT: The conventional fabrication of photothermally active materials involves expensive, time-consuming, or environmentally hazardous processes. A scalable and environmentally benign fabrication of free-standing photothermal materials through 2D printing is obtained using cellulose nanocrystal (CNC) aqueous shear-thinning inks containing plasmonic nanoparticles. Polyvinylpyrrolidone was used to stabilize 14.7 ± 1.1 nm spherical plasmonic AuNPs for enhanced compatibility with CNCs. The resulting inks, containing 1 wt % AuNPs to CNCs, were shaped into ~100 μm-thick lines, where CNC colloidal stability ensured homogeneous AuNP distribution within the printed materials. The suitability of printed materials for photothermal applications is demonstrated by a temperature increase of 12 °C after exposure to $\lambda = 520−525$ nm light over areas of 5×5 cm^2. Importantly, nondegradable synthetic petroleum-based polymers or multicomponent nanomaterials with serious environmental burdens are avoided. Printed materials show remarkable durability as evidenced by stable photothermia after 16 h of irradiation and no AuNP loss after immersion in stirring water for a week. Besides, given the nontoxicity of prepared materials, they may be disposed of at the end of their service life with negligible environmental impact. Therefore, this work provides cues to develop environmentally friendly photothermal microdevices that balance performance, material renewability, ease of processing, and degradability.

KEYWORDS: cellulose nanocrystal, Au nanoparticles, 2D printing, aqueous inks, shear thinning, photothermia
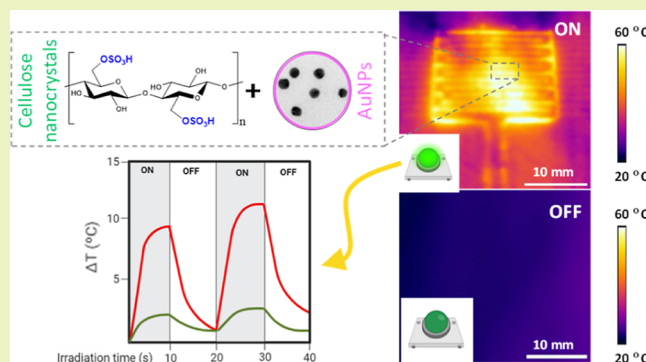
INTRODUCTION

The 21st-century society is witnessing unprecedented global challenges originating from the accumulation of nonbiodegradable waste in ocean and land environments, the depletion of finite nonrenewable/nonrecyclable resources, and the climate crisis. The current use of nonrenewable materials generates serious environmental burdens, including but not limited to large CO_2 emissions, air contamination, drinking water pollution, biodiversity loss, ocean acidification, and eutrophication.[1] As such, enormous efforts are being devoted to reach the climate-neutral goals set by the Paris Agreement and achieve a true circular economy by 2050.[2] Transitioning from the current linear fossil-based economy into a circular biobased economy that uses abundant, nontoxic, and renewable/biodegradable materials is a plausible solution to these challenges.[3]

Cellulose, the most common biobased polymer on earth, and its derivatives are receiving increasing importance as biosourced feedstock for multifunctional materials given their renewable nature, inherent biodegradability, ease of processing, and physicochemical properties. In particular, cellulose nanocrystals (CNCs), colloids that are isolated from native cellulose through a controlled cleavage of its amorphous regions,[4] are

highly versatile materials in terms of chiral self-assembly behavior,[5] optical properties,[6] mechanical response,[7] rheological behavior,[8] low cytotoxicity,[9] or energy storage.[10] These anisotropic biocolloids show diameters that range from 5 to 10 nm and lengths expanding from 100 to 1000 nm, and when isolated by sulfuric-acid-induced hydrolysis, their surface is decorated with hydroxyl (−OH) and anionic sulfate half-ester groups (−OSO₃⁻). This negatively charged surface provides good dispersion stability in water via repulsive electrostatic interactions.[11] Besides, aqueous CNC dispersions offer a strong shear-thinning behavior,[12] where the viscosities exponentially decrease with the shear rate. As a result, CNCs can tailor the rheological properties of the aqueous suspensions and confer a shear-thinning thixotropic behavior, allowing additive 2D and 3D manufacturing of multifunctional materials.

For example, CNCs have been recently used to develop shear-thinning inks for sustainable supercapacitor applications.[13] However, other technologically relevant fields such as photothermal applications remain open to exploration. In photothermia, heat is generated by active materials upon exposure to an external light source. Gold nanoparticles (AuNPs) are considered a prominent example of a material with photothermal properties given their localized surface plasmon resonance (LSPR).[14] So far, CNC/AuNP composites have been used as supports for enzyme immobilization in biocatalysis[15] or as an enzymatic glucose biosensor in human saliva.[16] An important property of AuNPs is their tunability on the absorbance wavelength through size and shape control.[17] The optical properties of AuNPs have been also exploited for the colorimetric detection of pathogenic DNA when capped onto CNCs[18] or in chiral plasmonic uses.[19] Besides, spherical AuNPs show a high photothermal conversion efficiency of 55−75%.[20] As such, AuNPs have been implemented into photothermal devices aimed at cancer therapy,[21] bacteria killing,[22] or biosensing platforms.[23] In spite of the increased environmental sustainability of AuNPs when compared with other LSPR-based photothermal materials such as palladium[24] or copper chalcogenide (Cu_9S_5) nanocrystals,[25] scarce reports exist on the use of CNC/Au composite materials for photothermia. Besides, Au has been recently identified as a noncritical raw material by the "Study on the Critical Raw Materials for the EU 2023" given its low supply risk and a relatively high end-of-life recycling input rate of nearly 30%.[26]

Citrate-stabilized AuNPs can be obtained through aqueous-based environmentally friendly wet chemical synthesis. Unfortunately, the high surface energy and low interaction of citrate−Au often result in aggregated nanoparticles when manipulated,[27] lowering the plasmonic absorbance and therefore, their efficiency in photothermal uses. Biocolloids such as CNCs, as well as other polymer and surfactant molecules, can tackle AuNP aggregation thanks to their charged surface and colloidal stability.[28] Besides, when AuNPs are combined with shear-thinning CNC-based aqueous inks, the resulting multifunctional solution material can potentially be processed by high-throughput fabrication routes. This solves the cost, scalability, and time-consuming issues of conventional fabrication routes of sensors or actuators by layer-by-layer,[29] solvent-casting,[30] or photolithography/sacrificial layer removal.[31]

Thereby, this work demonstrates that CNCs enable aqueous shear-thinning inks with embedded plasmonic AuNPs. In particular, CNCs at concentrations from 2 to 4 wt % can be used as a renewable and biodegradable viscosity modifier to enable environmentally benign water-based inks for additive manufacturing. The inks, containing 1 wt % plasmonic AuNPs with respect to CNCs, are processed into predesigned shapes onto mechanically flexible cellulosic substrates by screen printing, a time-effective and potentially scalable 2D printing technology. Microscopy observations reveal a lateral resolution below the millimeter where AuNPs remain well-distributed within the printed regions. The suitability of printed materials for photothermal applications is demonstrated by a temperature increase of 12 °C after exposure to λ = 520−525 nm light for 20 s. Overall, these results represent a step forward in the development of environmentally friendlier photothermal devices that rely on renewable and easily recyclable materials.

■ EXPERIMENTAL SECTION

Materials. CNCs at 8 wt % in an aqueous gel were provided by Blue Goose Biorefineries Inc. under the name BGB Ultra CNC (Saskatoon, SK, Canada). Polyvinylpyrrolidone (PVP) with a weight-average molecular weight (M_w) of 10,000 g·mol^{-1} (powder form) and $HAuCl_4$·$3H_2O$ (≥99.9% trace metals basis) were purchased from Sigma-Aldrich. The cellulose acetate film having a thickness of 25 μm was obtained from Goodfellow Cambridge Limited (Huntingdon, UK).

Synthesis of AuNPs. AuNPs were synthesized through an adapted Turkevich method.[32] Basically, an aqueous solution of $HAuCl_4$·$3H_2O$, 95 mL at 0.5 mM, was brought to a boil. 5 mL of sodium citrate at 1 wt % was quickly added under magnetic stirring and left to react for 15 min. The solution was left to cool down to room temperature and stored in a fridge until further use. For the ligand exchange of the NPs, a solution of PVP at a concentration of approximately 1 mg·mL^{-1} was added dropwise to the NP solution at room temperature and left stirring for at least 1 h. The amount of added PVP was calculated to be 60 molecules per nm^2 of the nanoparticle surface based on the transmission electron microscopy (TEM) diameter and the approximate NP concentration measured by UV−vis (0.5 mM corresponds to 1.2 absorbance units at 400 nm). The NP solution was then centrifuged at 14,000 rpm and the supernatant was removed. The NPs were redispersed in ultrapure water and centrifuged once more. Finally, ultrapure water was added to obtain a concentrated solution of around 30 mM.

Ink Preparation and Its Processing. First, aqueous CNC inks comprising different CNC concentrations were prepared. A given amount of CNCs was weighted for the initial 8 wt % aqueous gel, and DI water was added to obtain concentrations of 2, 3, and 4 wt %. The solution is dispersed using a mechanical stirrer for 1 h followed by an ultrasound bath for 1 h. Photothermal inks were prepared upon the incorporation of AuNPs into the 2, 3, and 4 wt % CNC inks. The concentration of AuNPs within the ink was set at 1 wt % as it provides enough photothermal response with no marked changes in ink viscosity.

For 2D printing, the inks were forced through a screen mesh (77 line·cm^{-1}; thread diameter of 48 μm) toward a cellulose acetate substrate upon the application of pressure using a semiautomatic DX-3050P vertical electronic drive screen printing instrument from Shenzhen Dstar Machine Co. The cellulosic substrate was set at 10 mm, while the squeegee angle with respect to the screen was set at 30°. For all the samples, the printing speed was optimized at 13.6 cm·s^{-1}. Printed features were dried at room temperature for 2 h.

Characterization. TEM images were acquired in a JEOL 1400 Plus operating at 100 kV. AuNP solution (∼4 μL at 0.1 mM) was deposited on a carbon-coated TEM grid and left to dry. The NP morphological features were analyzed with the ImageJ software package. Field-emission scanning electron microscopy (FE-SEM) analyses were carried out using a Hitachi S-4800 at an acceleration voltage of 5 kV. Before imaging, samples were sputtered with a 10 nm-thin gold−palladium layer. SEM coupled with energy-dispersive X-ray spectroscopy (EDX) analyses were performed on a DSM 982 Gemini instrument (Zeiss).

AuNP absorbance in diluted aqueous dispersions was obtained in a Cary 60 (Agilent) over the 300−1100 nm range in a standard plastic macro-cuvette. UV−vis diffuse reflectance spectroscopy (DRS) was performed in a fiber optic spectrometer (AvaSpec-ULS2048CL, Avantes) equipped with an AvaLight-DHc light source and a 7-fiber reflection probe positioned at 45° of the sample. Barium sulfate was used as a blank reference, assuming a 100% reflectance. Finally, the reflectance of the substrate was subtracted from that of the printed lines. Thermogravimetric analysis was conducted in a TGA METTLER TOLEDO 822e instrument using alumina pans with a nitrogen flux of 50 mL·min^{-1} for a sample of 9 mg.

The rheological properties of the printing inks were evaluated in a Brookfield DV2T Touch Screen viscometer with cone−plate geometry (CPA-52Z cone, 3° cone angle, 1.2 cm cone radius). Measurements were performed in the 2-to-100 s^{-1} shear rate range.
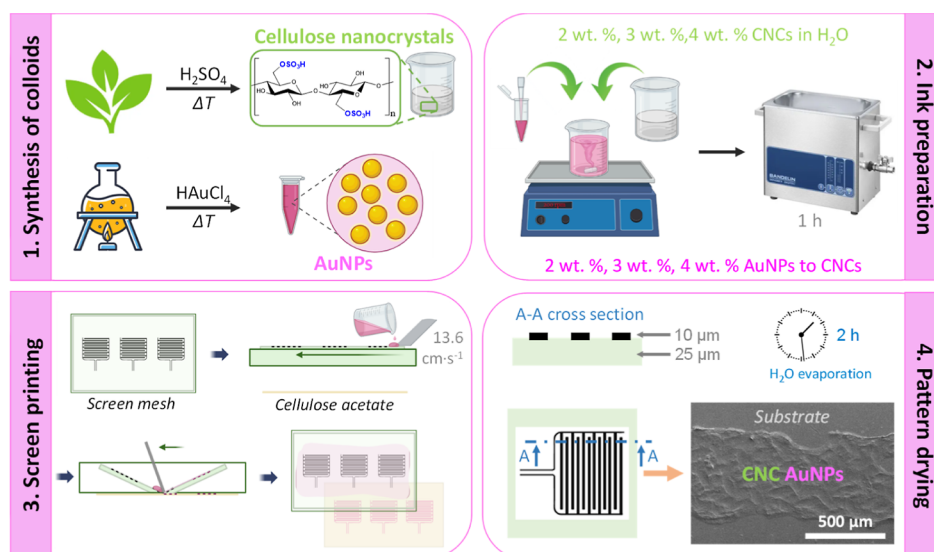
Figure 1. Schematic of the fabrication of the photothermal printable microdevice through screen printing showing the main steps as (1) CNC and Au colloid synthesis from biomass and the Au salt; (2) aqueous ink preparation; (3) screen printing steps at a squeegee speed of 13.6 cm·s^{-1}; and (4) schematic of the printed patterns obtained after 2 h of drying at room temperature, where the morphology of the printed material (CNC/AuNPs) onto the substrate is shown.

Powder X-ray diffraction (XRD) patterns were obtained with a D8 DISCOVER diffractometer in reflection mode by using Cu Kα radiation (45 kV, 40 mA). Fourier transform infrared (FTIR) spectroscopy analyses in attenuated total reflection (ATR) mode were performed by using a Jasco FT/IR-6100 spectrometer (diamond ATR). The spectra were collected after 32 scans in the range of 3800−800 cm^{-1} with a resolution of 2 cm^{-1}.

The mechanical behavior of screen-printed films was studied by uniaxial tensile tests using a universal testing machine (Trapezium Shimadzu AGS-X) equipped with a 100 N load cell at a deformation rate of 1 mm·min^{-1}. 50 mm long and 10 mm width specimens with a thickness of ∼25 μm were used. Mean average value and standard deviation Young's modulus (E) (from 0.5 to 1% strain region) and stress and strain at break (σ_b and ε_b, respectively) were determined from five measurements.

For photothermia, the screen-printed materials were supported on a flat glass positioned around 1 cm above the LED lamp. The LED lamp, which illuminated from below the sample, consisted of a green light LED panel (Chanzon, 100 W, and λ = 520−525 nm) placed on a heat sink and covered with a 60° collimating lens and a dc power source. The light power at the sample position was measured using a power sensor (S425, Thorlabs) and controlled through the LED current to obtain a final irradiance of 0.2 W·cm^{-2}. The temperature was measured from the top using a thermal camera (FLIR E4) and evaluated with the FLIR tools + software package.

■ RESULTS AND DISCUSSION

As summarized in Figure 1, the aim of this work was the fabrication of printable photothermal materials with predesigned shapes by a quick yet effective approach. The obtained materials were irradiated with LED light. A λ of 520−525 nm was chosen to fit the wavelength of maximum absorbance of the nanoparticles, which also corresponds to the maximum of received sunlight, expanding its possible applicability. The temperature increase of the printed substrate at different locations and times was monitored. Colloidal gold was used for photothermal energy conversion given its high photothermal conversion efficiency around their LSPR.[33] For the spherical AuNPs, the wavelength of absorbance takes place at around 500−600 nm depending on the NP size.[34] This wavelength can be further red-shifted by modifying its shape (nanorods,

nanostars, bipyramids, etc.); however, those nanoparticles tend to reshape toward spherical morphologies under the photothermal stimulus.[35] In this work, spherical AuNPs were used given their increased stability when increasing the temperature (vs. nanostars, for instance) and their characteristic wavelength of maximum absorbance at ∼520 nm, making them useful for applications where sunlight is the power source as it corresponds to the region of sunlight's maximum emission.

Spherical citrate-coated AuNPs were synthesized by the Turkevich method. The low citrate affinity to Au made the NPs easily aggregate when manipulated, both in purification and in mixing with CNCs. To solve it, the NPs were coated with PVP, which provided high colloidal stability in water. Next, AuNPs were incorporated into shear-thinning inks enabled by CNCs. The concentration of CNCs in the ink was tuned from 2 to 4 wt %. The inks were processed by screen-printing onto 30 μm-thick free-standing cellulose acetate films, which were irradiated by a green LED to investigate temperature changes with the help of a thermal camera. Thanks to the renewability and biodegradability of the cellulose acetate substrate and the CNC viscosity modifier,[36] together with the noncytotoxic/biocompatibility of Au colloids,[37] the fabricated photothermal materials could be potentially applied into transient/degradable devices, undergoing controlled biodegradation processes to leave nontoxic products after a period of stable operation.[38] As such, these materials could be disposed of at the end of their service life, enabling their implementation into sustainable agricultural sensing, smart packaging, or biomedical actuator applications.

AuNP Synthesis. First, citrate-coated AuNPs were synthesized in aqueous media by using citrate as a stabilizing and reduction agent. As shown in Figure 2a, the formed NPs were observed by TEM (Figure S1 for a lower magnification image), revealing a spherical shape with an average diameter of 14.7 ± 1.1 nm (particle size distribution histogram in Figure S2). Water-dispersed citrate-coated AuNPs presented a maximum absorption peak at 519 nm (Figure 2b) corresponding to the nanoparticle LSPR dipolar mode. After the ligand exchange of citrate by PVP, the AuNP solution plasmonic peak
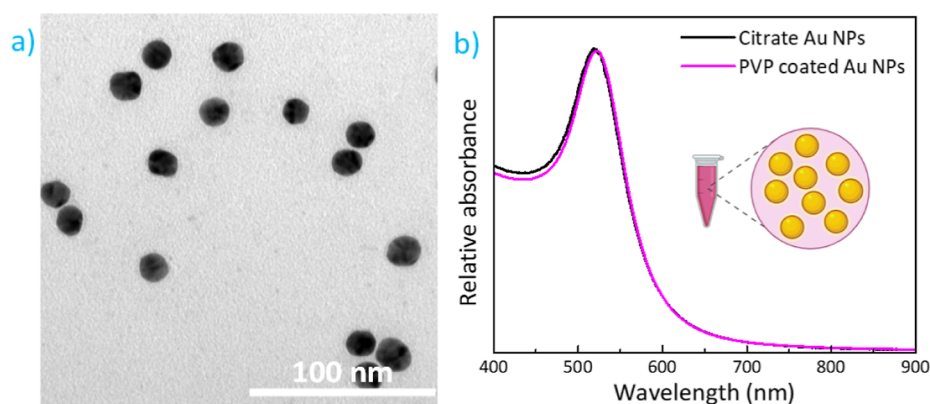
Figure 2. (a) High-magnification TEM image of PVP-coated AuNPs and (b) UV−vis spectra of the solution of citrate and PVP-coated AuNPs with a scheme showing their dispersion within an Eppendorf tube.
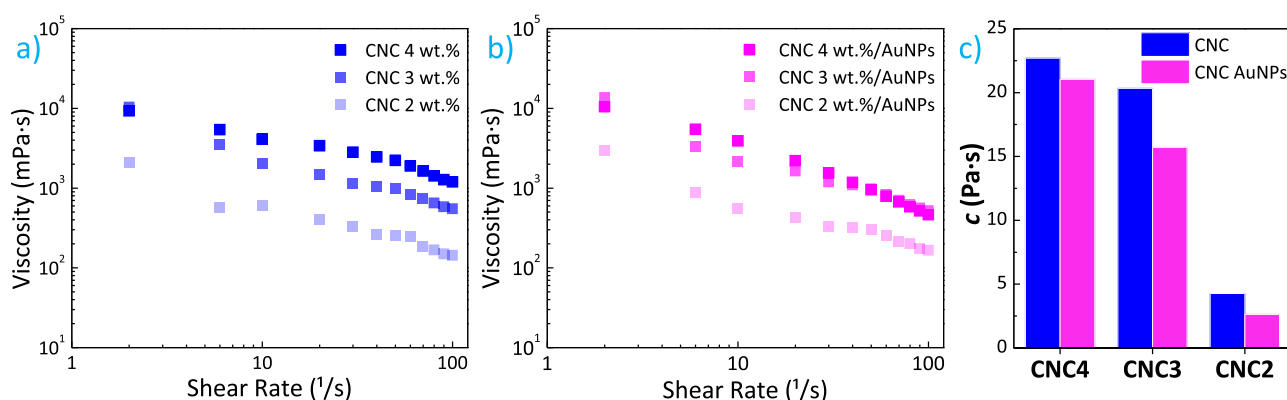

Figure 3. Viscosity of (a) bare CNC inks and (b) CNC/AuNP inks as a function of the applied shear rate. (c) c flow coefficient based on the Ostwald−de Waele model.

underwent a red shift of 3 nm (to 522 nm), as a consequence of the refractive index change around the Au core.[39] Given the improved water stability of the PVP-coated AuNPs, after modification, these nanoparticles could be easily mixed in aqueous solutions without any further change. Thermogravimetric analysis in Figure S3 reveals a PVP concentration of 5.1 wt % in the AuNPs, where a thermodegradation event originating from PVP is seen in the 240−550 °C range.

Ink Formulation. The viscosity of the aqueous CNC inks was evaluated at shear stresses (2 to 100 s^{-1}) characteristic of the screen-printing process. Figure 3a shows the viscosity as a function of the applied shear rate for 2, 3, and 4 wt % bare CNC aqueous inks. The formulations presented viscosity values ranging from 3000−15,000 to 150−1000 mPa·s when the shear rate increased from 2 to 100 s^{-1}. A positive correlation between CNC concentration and viscosity was observed for the whole shear-rate range studied given the physical gelling abilities of nanocelluloses including microfibrillated cellulose and cellulose nanofibrils and the hydrogen bonding occurring between adjacent CNCs. This result originates from the formation of an intricate network of physically entangled CNCs at higher concentrations, which offer a higher resistance to flow. Thereby, for a given shear rate, the 4 wt % CNC ink shows a nearly 3-fold increase in viscosity when compared with the 2 wt % CNC ink, which presents viscosity values of 3000 and 160 mPa·s when the shear rate increases from 2 to 100 s^{-1}, respectively.

Importantly, the linear negative relationship between the viscosity and shear rate (on a log−log plot) indicates a shear-thinning behavior of the inks. This shear-thinning behavior is the preferred behavior for 2D and 3D additive manufacturing technologies as it avoids the undesired flow of the inks when no shear forces are applied but enables its processing when external forces are applied presenting lower viscosity upon the application of external forces.[8,12,40] Then, after screen printing, no shear forces are applied so that the transferred wet layer of material can keep its shape with no uncontrolled spreading (high viscosities). The curves in Figure 3b for the hybrid CNC/AuNP inks presented reduced viscosities when compared with bare CNC inks, suggesting that even a low concentration of AuNPs (1 wt % vs. CNC content) is able to disrupt intermolecular hydrogen-bonding interactions between neighboring CNCs.

Considering the viscosity curves in Figure 3a,b, hybrid Au inks containing 3 or 4 wt % CNCs (over the CNC/AuNP 2 wt %) are particularly interesting for printed applications as they offer viscosities within the recommended window for screen printing.[41] Besides, the 4 wt % ink has a yield shear stress (the minimum shear stress required to disrupt the CNC physical percolating network and initiate flow) of ∼49 Pa, a typically required value for screen printing with high printing resolution.[42] These results highlight the suitability of CNCs to act as ink modifiers at relatively low concentrations, over water-soluble cellulose derivatives (methylcellulose, hydroxypropyl cellulose, and sodium carboxymethyl cellulose), which showed reduced viscosities at 10 s^{-1} shear rate.[43] The linear relationship between shear rate and viscosity observed indicates that the inks are within the power law region (at
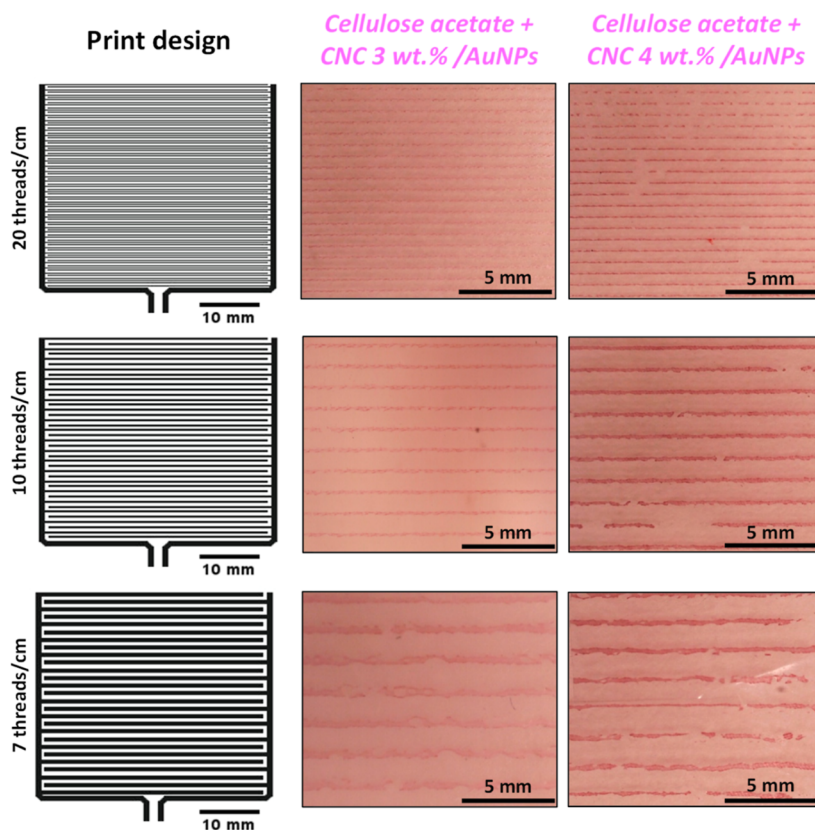
Figure 4. Optical photographs showing a magnified macroscopic appearance of printed patterns using CNC 3 wt %/AuNP and CNC 4 wt %/AuNP inks for three different print patterns. Screen-printing mesh counts (threads per cm) are included.

low rates, the shear is too low to be impeded by entanglements and the viscosity takes a constant value, while at high shear rates, the CNCs will remain entirely disentangled so the viscosity value plateaus). Accordingly, the Ostwald−de Waele relationship, often used to analyze the fluid behavior of non-Newtonian fluids,[44] has been applied to further evaluate the shear-stress/shear-rate curves as

$$\tau = c \cdot D^p \tag{1}$$

where τ accounts for the viscosity, D is the shear rate or the velocity gradient, and c and p represent the flow coefficient and the power-law index (unitless) obtained from the linear fit of power-law approximation to the experimental data, respectively. It is to be noted that fitting to this power-law model is appropriate when the obtained data (for a shear-rate region) remain within the shear-thinning regime. As summarized in Figure 3c, c values decrease from 22.7 to 4.3 Pa·s when CNC concentration is lowered from 4 to 2 wt %, respectively. Besides, AuNP incorporation reduces the c value, in agreement with the viscosity decrease observation arising from hydrogen-bonding disruption. The observed c values are notably above the 0.9−4.1 Pa·s showed by water-soluble cellulose derivatives, suggesting an improved printability enabled by CNCs.[43] Besides, as high c values are correlated with increased pseudoplasticity (shear-thinning behavior), the Ostwald−de Waele relationship suggests that hybrid inks having CNC concentrations of 3 and 4 wt % are better suited for 2D printing.

Screen Printing. The CNC/AuNP inks were screen-printed onto a 30 μm-thick cellulose acetate film by using a thread diameter of 48 μm. Cellulose acetate fulfills the mechanical and optical requisites for 2D printing substrates while also offering a renewable material as opposed to conventionally used petroleum-derived materials such as polyethylene terephthalate.[45] Patterns with different line spacings and line widths were applied to prove the suitability of the CNC/AuNP inks for 2D printing. A visual inspection of the optical photographs of printed materials using meshes with three different line widths in Figure 4 for the CNC 3 wt %/AuNP ink shows a good screen-printing fidelity with appropriate line uniformity and good parallelism between the lines, in accordance with the results shown by Kokol et al. for microfibrillated cellulose inks.[46] However, areas not completely covered by CNC/AuNPs appear during the printing process for the ink containing a CNC concentration of 4 wt %. This can be explained by a larger viscosity of the ink blocking the printing mesh (especially for the mesh having 20 thread·cm^{-1}). Besides, surface tension differences at larger CNC concentrations reduce its affinity with the CA substrate and result in agglomeration of the printed droplets, especially noticeable when larger amounts of material are printed (low thread densities, Figure 4, bottom right). In spite of these difficulties, it is noteworthy that CNC inks facilitate the controlled deposition of photothermally active AuNPs with no need for petroleum-based surfactants or solvents.

The width of the printed patterns was measured and contrasted with the line width of the printing mesh, and the results are summarized in Figure 5 (further details are given in Table S1). Overall, printed lines are thinner than the original mesh size in the screen pattern for all the compositions, indicating a volume shrinkage (driven by the capillary forces induced by CNCs) of the material once the ink diffuses
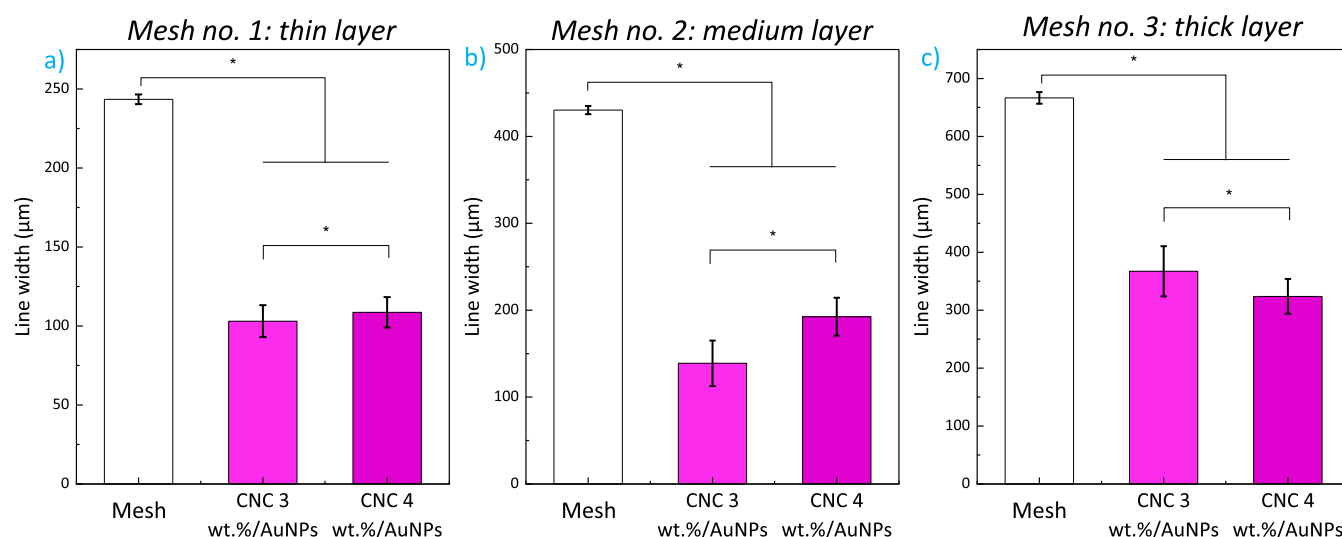
Figure 5. Bar diagrams showing line width average and standard deviation values for the three screen or mesh patterns used: (a) thin layers; (b) medium layers; and (c) thick layers. The CNC 3 wt %/AuNP and CNC 4 wt %/AuNP inks have been used and the statistics are based on 100 measurements using ImageJ. * = subject to uncertainty given the poor print quality. The ANOVA test showed a significant difference among the groups (*p value < 0.05).

throughout the screen. The analysis of variance (ANOVA) was applied to determine whether or not statistical differences exist among the data. With $p < 0.05$, statistical differences among the data are found. Besides, Tukey's honestly significant difference (HSD) test indicates that all the printing meshes yield line widths that are statistically different. For both the thin and medium mesh lines, the volume shrinkage is more pronounced (thinner lines) for the diluted ink (CNC 3 wt %/AuNPs) as larger CNC concentrations enable an increased spreading of the ink breadthways onto the cellulose acetate substrate. However, the opposite trend is observed when the mesh having thicker lines is used, which could probably originate from a loss in print fidelity due to excess material deposited (as observed in Figure 4, bottom-right image).

As seen in Figure 6, the morphology of the printed material using the mesh with the thinnest lines was further analyzed by FE-SEM. The FE-SEM surface image shows line widths down to 93 μm, very close to the ones measured by optical microscopy, with good shape fidelity thanks to the shear-
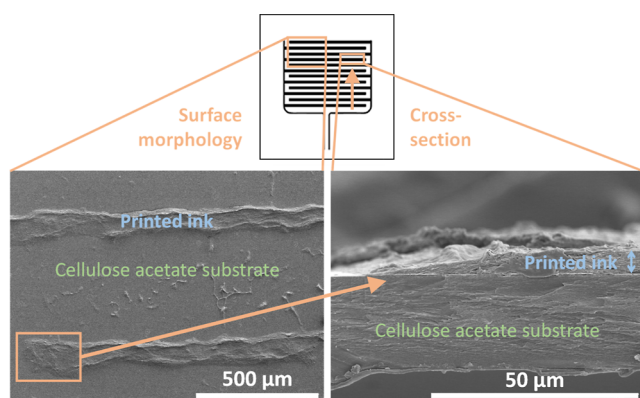

Figure 6. Representative FE-SEM micrographs showing the surface (left) and cross-section (right) morphology of the prints using the CNC 3 wt %/AuNP ink. The double-headed blue arrow represents the height of the printed CNC 3 wt %/AuNP material. The area of the printed region (represented at the top) is 4 × 8 cm^2.

thinning behavior enabled by CNCs (offering an easy pass through the mesh upon shear application by the squeegee) and a rapid elastic recovery of the zero shear viscosity (printed patterns do now flow onto the cellulose acetate substrate once printed).[47] The cross section shows an 11 μm-thick profile of the CNC 3 wt %/AuNP material with no delamination or detachment between the printed phase and the cellulose acetate substrate (note that the cross-section image represents the end of the printed layer as shown in Figure 4, left). Likewise, a good interfacial compatibility between the substrate and the ink is obtained as proven by the detailed SEM micrograph in Figure S4 (no voids between CA and the deposited inks are observed at a magnification of 25k). This result originates from the similarities in their chemical composition; the cellulose acetate substrate and the CNC-based ink remain tightly bound via hydrogen-bonding interactions at the interface (OH groups in the ink and OH/ acetate groups on the substrate).[48] As depicted in Figure S5, the CNC/AuNP inks screen-printed onto conventional filter paper having micrometer-sized pores (Whatman grade 4) offer a good shape fidelity, reflecting the adaptability of the materials developed.

High-magnification FE-SEM images in Figure S6 reveal a nanoporous morphology on top of the printed patterns. These nanopores offer an interesting platform for sensing applications as the available surface area to interact with potential analytes is enlarged. The pore diameter ranges from 21.1 ± 11.2 nm to 17.3 ± 6.9 nm for the CNC 3 wt %/AuNP and CNC 4 wt %/AuNP samples, respectively, while the surface coverage of the pores decreases from 14.7 to 11.1% (Table S2, statistics obtained using ImageJ). Such pores may have been formed upon water evaporation from the inks, where increased CNC fractions (and thus a lower water fraction) yield smaller and less-abundant pores.

The elemental mapping in Figure S7 shows the spatial distribution of AuNPs within the CNC ink matrix after printing. No sign of aggregated AuNPs along the printed lines could be observed even at high magnifications. This homogeneous AuNP distribution is ascribed to the following
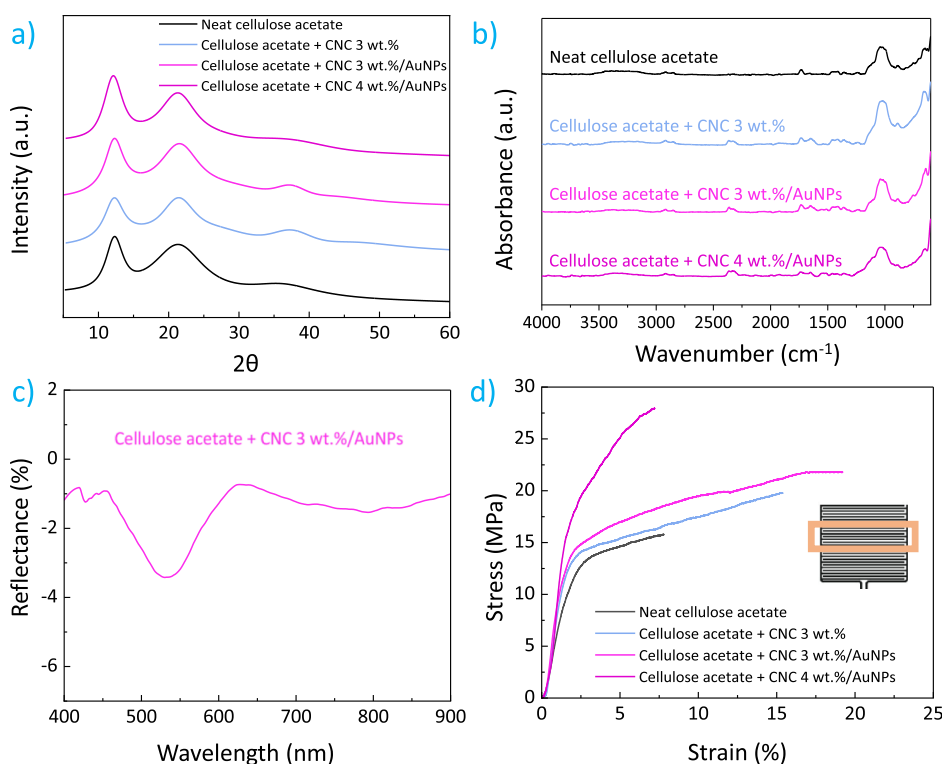
Figure 7. (a) XRD; (b) ATR-FTIR; and (c) UV−vis diffuse reflectance spectra of the CNC 3 wt %/AuNP printed material; and (d) tensile stress−strain curves for the printed materials (note that the most representative curve from the five measurements performed at each composition is shown). The inset shows tensile testing samples obtained from the printed patterns.

reasons. The dispersions of CNCs present highly negatively charged groups at the CNC (deprotonated sulfate half-ester; ζ-potential of −40 mV approximately) and AuNP (due to PVP; ζ-potential of −10 mV approximately) surfaces. As a result, electrostatic repulsion forces between the colloids are achieved,[11] which in combination with the steric repulsion of the AuNPs provided by the PVP coating provide a good colloidal stability in the inks. Besides, the abundant hydroxyl and sulfate ester functional groups onto CNCs can also stabilize AuNPs in the dried patterns obtained upon screen printing due to the coordinate bonding of AuNPs with the hydroxyl oxygen of CNCs.[49,50] Besides, the stability of the printed ink onto the cellulose acetate substrate was tested by maintaining the material immersed in stirring distilled water for 7 days. After this period, the supernatant was analyzed by UV−vis (Figure S8), and no traces of AuNPs were detected in the medium, indicating that the CNC matrix holds the material together and avoids undesired AuNP loss into the environment. As such, results demonstrate the advantages of CNC inks over water-soluble cellulose derivative inks such as methylcellulose or hydroxypropyl cellulose, which require extensive preparation times for dissolution and removing lumps and persistent bubbles (CNC inks can be rapidly prepared by simply applying an ultrasonic bath for 5 min) and yield reduced shape fidelity characteristics.[43]

Optical and Mechanical Properties. Printed materials are semicrystalline as indicated by the XRD pattern in Figure 7a, where broad diffraction peaks originating from the semicrystalline character of cellulose acetate and CNCs coexist with a broad amorphous halo (no traces of AuNPs are seen given its low concentration). The ATR-FTIR spectra in Figure 7b show the characteristic peaks of cellulose acetate with no sign of CNCs or AuNPs because of their low concentration in

the whole sample (a ratio of 95:5 for substrate/ink is estimated according to the analysis area; ATR crystal having a 1.8 mm diameter; <2 μm penetration depth). Besides, the chemical similarities between CNCs and cellulose acetate also make ink identification difficult. In any case, the observed bands for all the samples correspond to the C−H bending and C−O stretching vibrations of acetyl groups (1370 and 1220 cm^{-1}, respectively), the symmetric C−O−C stretching of cellulose (1035 cm^{-1}), and the acetate methyl groups at 904 cm^{-1}.[51]

The optical properties of printed materials are relevant for practical applications. Thereby, UV−vis DRS in the 400−900 nm range was conducted for the CNC 3 wt %/AuNP printed material, and the results are shown in Figure 7c. Due to the small line size and thickness of the printed lines, only a small reflectance variation was observed. Equally, in absorbance spectroscopy, more than 98% of the light was transmitted. As a result, materials with optical transparencies above 98% at the visible-light region (λ = 540−560 nm, ASTM D1746-03) are achieved (Figure S9). On the other hand, a clear plasmonic peak was observed with a maximum in the 530−540 nm region, provided by the AuNPs and very similar to the AuNP solution. The small red shift with respect to the solution, probably due to the change in refractive index, is indicative of the good dispersion of the AuNP in the CNC matrix. These results confirm that the nanoscale character of the viscosity modifier (CNCs), together with the low concentration of AuNPs used, enables materials potentially suitable for photothermal applications with a relatively high degree of transparency such as antifogging.[52]

Besides, low CNC concentrations yield materials that maintain or even improve the mechanical properties of neat cellulose acetate substrates as proven by the uniaxial stress−strain curves in Figure 7d. In particular, the elongation at break
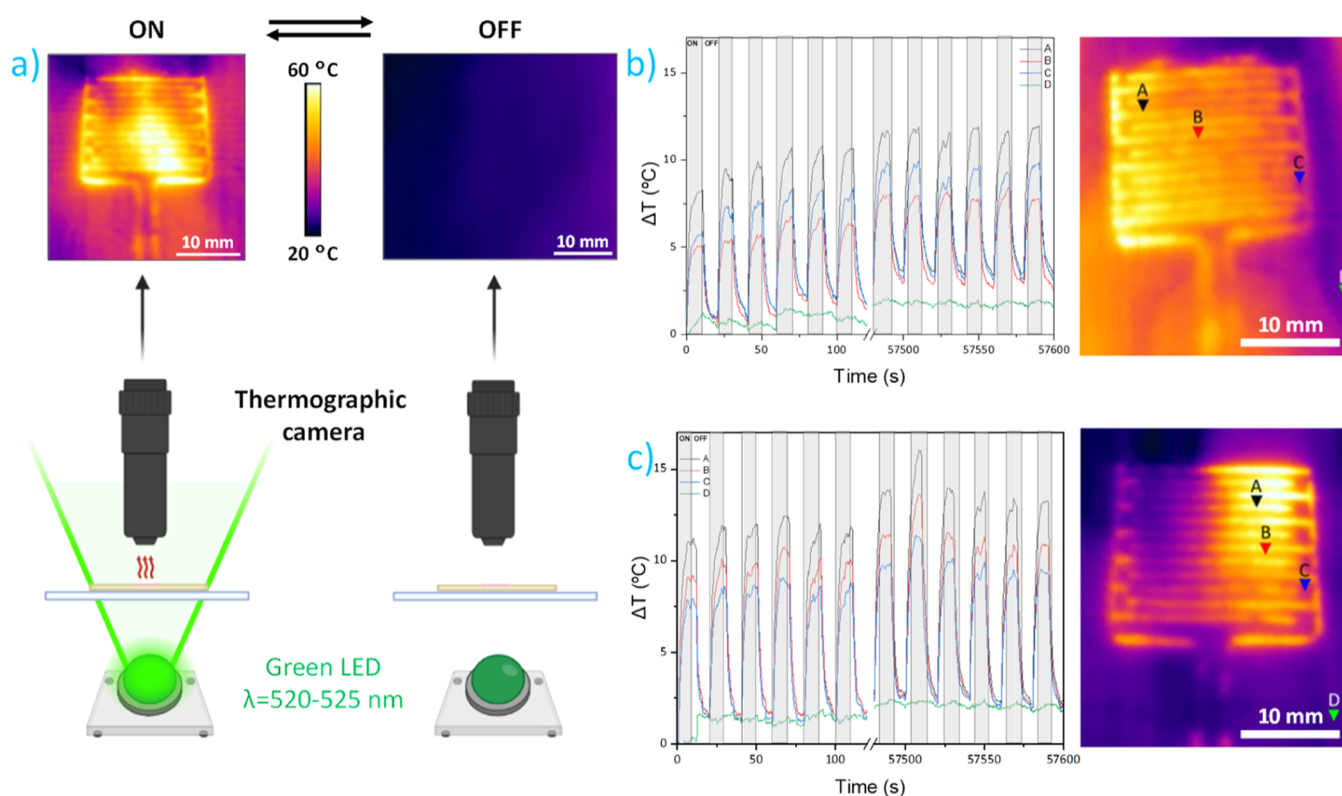
Figure 8. (a) Conceptual illustration or the evaluation of the photothermal effect in the printed materials. Photothermal effect of the printed materials upon irradiation for 16 h or 57,600 s: (b) CNC 3 wt %/AuNP inks and (c) CNC 4 wt %/AuNP inks. The corresponding photograph from the thermal camera is provided, which shows the specific location for the colored curves on the left.

increases from 7.8 ± 3.9% of cellulose acetate to a maximum of 20.9 ± 12.5% for the printed material using the CNC 3 wt %/AuNP ink (see Table S3 for additional details). An additional increase in the CNC concentration notably stiffens the material and reduces the elongation at break to 4.7 ± 1.8%, while Young's modulus increased by 77% (from 774.7 + 178.2 MPa of cellulose acetate to 1375 + 162.5 MPa), indicating a mechanical reinforcing impaired by the CNCs.[11] The results show that the CNC 3 wt %/AuNP ink is the most appropriate formulation to keep a good balance of mechanical flexibility and strength.[53]

Photothermal Response. The light-to-heat conversion of plasmonic nanoparticles can be exploited to develop free-standing photothermal materials with many technological applications.[54] As shown in Figure 8a, a homemade system was designed to perform photothermal tests of printed materials. The printed cellulose acetate substrate was irradiated with LED light at λ = 520−525 nm and a relatively low irradiance power of 0.2 W cm^2 for different periods of time and the temperature distribution at different locations was monitored using a thermographic camera as seen in Video S1 for the CNC 4 wt %/AuNP ink. A minimal interference with the direct illumination of light is observed, given the high optical transparency of the substrate in the region of interest.

The dynamic response of the local temperature difference (ΔT), defined as the difference between the measured temperature and the initial temperature, at different film locations is shown in Figure 8b,c. A steep temperature increase on the prints (location A) that quickly turns into a plateau is observed upon irradiation, while the temperature rapidly decays once the light illumination is stopped. The rapid light-

to-heat conversion demonstrated by a ΔT value of 12 °C solely after 20 s of irradiation is due to the LSPR of AuNPs originating from the collective oscillation of conduction electrons in response to incident light. This plasmon resonance causes the NPs to strongly absorb and scatter light at the resonance wavelengths, where the absorbed light generates heat through the damping of the plasmons.[54] On the contrary, in the absence of CNC/AuNP printed regions (location D, control), a notably lower ΔT of ~2 °C is observed, which may probably originate from the heat absorption of the substrate under the sample. Finally, for the regions between lines B and C, a concomitant increase in temperature was also observed due to the heat transmission through the cellulosic substrate, which is highly attenuated as we move farther from the photothermal lines ($\Delta T_A > \Delta T_B > \Delta T_C > \Delta T_D$).

A secondary temperature increase of nearly 2 °C that stabilizes in the form of an inverse exponential after ~1.5 min is achieved (a baseline stabilization is seen due to a saturation effect)[55] given the fact that the material cannot be fully cool down during the 20 s in the Off mode. However, as such a temperature increase is well below the glass transition or thermodegradation temperatures of both cellulose acetate and CNCs (~200 and ~250 °C, respectively),[56,57] we do not expect detrimental effects that would reduce the operating lifespan of the material. In fact, a consistency upon 6 successive cycles of irradiation (illumination for 20 s followed by 20 s dark) with no photobleaching is observed, indicating an extended durability of the printed materials. Importantly, the obtained temperature increases are suitable for hyperthermia applications, where temperatures of 41−47 °C are required for tumor destruction.[58] Besides, these materials may be also

adequate for optically transparent coatings with anti-icing properties due to a heating effect[59] or for coatings with antifogging and defogging abilities upon exposure to visible light.[52]

To gain a better picture of these findings, we turned to the literature (Table S4 provides further details on state-of-the-art examples). As a matter of fact, a ΔT value of 18.1 °C has been reported after a one-sun irradiation of polytetrafluoroethylene/ $Ti_3C_2T_x$ MXene membranes during 60 s,[60] while a ΔT of ~38 °C has been seen in AuNR@graphene oxide nanohybrids dispersed in water irradiated during 300 s at λ = 808 nm (300 mW),[61] and a ΔT of ~30 °C has been achieved at a λ = 800 nm irradiation of gold nanostars (irradiance of 14 W·cm^2) during 100 s[62] However, it should be considered that these reported works present several drawbacks regarding their implementation information on environmentally sustainable devices:

- First, synthetic petroleum-based polymers are used for nanoparticle immobilization, representing a possible nondegradable source once the end of life has been reached.[63]

- Second, multicomponent nanomaterials such as titanium carbide MXenes are applied, with serious environmental burdens upon fabrication, toxicity associated with surface chemistry, and secondary contamination resulting from their degradation.[64]

- Third, photothermia is obtained upon dispersion of NPs in water solutions, contaminating the media with nano-sized objects whose removal is challenging.[65]

The photothermally active inks developed here could be potentially used in 3D printing applications such as direct ink writing. To that end, the zero shear viscosity of the inks should be enhanced so that undesired flow events after printing are avoided (ensuring adequate shape fidelity).[12,66,67] Accordingly, we estimate that the CNC concentration should be increased up to 10−40 wt % to develop suitable inks for 3D-printed photothermia uses. Overall, the developed photothermal materials have great fabrication versatility and could be exploited in security printing for anticounterfeiting uses based on IR light,[68] smart labels, photodynamic−photothermal antibacterial therapy,[69] or photothermal catalysis among others.[70] With these merits, our free-standing cellulose-based hybrid films offer a comparable photothermal activity but with the additional big advantage of material renewability, ease of fabrication/processing, and no loss of active AuNPs into the environment as they remain anchored to the cellulose acetate film by the CNC matrix. As such, these results provide a proof of concept for the applicability of CNC/AuNP inks onto biodegradable materials for photothermal devices.

CONCLUSIONS

This work addresses the conventional nonscalable, time-consuming, and environmentally hazardous fabrication of photothermally active materials upon the preparation of water-based CNC inks with incorporated plasmonic AuNPs. Photothermally active predesigned 2D patterns were prepared onto mechanically flexible cellulosic substrates using screen printing. 14.7 ± 1.1 nm plasmonic spherical AuNPs synthesized by a wet chemical method were surface-coated with PVP to improve their compatibility with aqueous solvents. Inks having 2, 3, and 4 wt % CNCs presented a decrease in the viscosity from 3000−15,000 to 150−1000 mPa·s when the

shear rate increased from 2 to 100 s^{-1}. The spindle shape of CNCs, together with their negatively charged surface decorated by anionic sulfate half-ester groups ($-OSO_3^-$), enables a shear-thinning behavior of the inks that translates into a homogeneous AuNP dispersion upon printing, even for line widths of ~100 μm. When using the 3 wt % ink containing 1 wt %AuNPs, the materials present a plasmonic absorption at around 530 nm while enabling the transmission of >98% light throughout the film (resulting in nearly transparent materials) and are mechanically resistant (strain at break of 20.9 ± 12.5% and Young's modulus of 927.0 ± 84.9 MPa), particularly interesting for areas such as flexible electronics. Besides, the developed materials show a temperature increase of 12 °C after exposure to λ = 520−525 nm light for 20 s.

Remarkably, the photothermal effect is obtained over surface areas extending up to 5 × 5 cm^2 with no need for nondegradable synthetic petroleum-based polymers or multi-component nanomaterials with serious environmental burdens upon fabrication. As a result and benefiting from the renewable and biodegradable viscosity-modifier role of colloidal CNCs, the aqueous shear-thinning photothermally active materials developed here have great potential for advanced sensing, actuators, or biomedical fields. Printed materials are durable for over 16 h of irradiation and highly resistant to water. As a result, this work provides cues for the development of photothermal devices that maintain a good balance between ease of processing, performance, material renewability, and potential biodegradability, enabling their implementation into sustainable applications.

■ ASSOCIATED CONTENT

Data Availability Statement

All the data used to support the findings of this study are included in the article.

ⓢ Supporting Information

The Supporting Information is available free of charge at https://pubs.acs.org/doi/10.1021/acssuschemeng.3c05599.

> TEM micrograph of AuNPs and their corresponding size distribution plot, thermogravimetric analysis, high-magnification SEM observations together with EDX, optical photographs of the 2D-printed designs, UV−vis transmittance spectra of the washing medium and the printed material, and tables summarizing the printed line widths, pore size characteristics, and main mechanical parameters of printed materials and literature comparison (PDF)

> Video acquired using a photothermal camera showing the temperature increase (AVI)

■ AUTHOR INFORMATION

Corresponding Author

Erlantz Lizundia − *BCMaterials, Basque Center for Materials, Applications and Nanostructures, Leioa 48940, Spain; Life Cycle Thinking Group, Department of Graphic Design and Engineering Projects, Faculty of Engineering in Bilbao, University of the Basque Country (UPV/EHU), Bilbao 48013, Spain;* ⓞ orcid.org/0000-0003-4013-2721; Email: erlantz.liizundia@ehu.eus

Authors

Marta García-Castrillo — *BCMaterials, Basque Center for Materials, Applications and Nanostructures, Leioa 48940, Spain;* orcid.org/0000-0002-1243-8662

Javier Reguera — *BCMaterials, Basque Center for Materials, Applications and Nanostructures, Leioa 48940, Spain;* orcid.org/0000-0001-5110-5361

Complete contact information is available at:
https://pubs.acs.org/10.1021/acssuschemeng.3c05599

Author Contributions

The manuscript was written through contributions of all authors. All authors have given approval to the final version of the manuscript.

Notes

The authors declare no competing financial interest.

■ REFERENCES

(1) Porzio, J.; Scown, C. D. Life-Cycle Assessment Considerations for Batteries and Battery Materials. *Adv. Energy Mater.* **2021**, *11* (33), 2100771.

(2) European Commission. Circular Economy Action Plan 2020, 2023. https://environment.ec.europa.eu/strategy/circular-economy-action-plan_en (accessed on October 2023).

(3) Johnson, C.; Ruiz Sierra, A.; Dettmer, J.; Sidiropoulou, K.; Zicmane, E.; Canalis, A.; Llorente, P.; Paiano, P.; Mengal, P.; Puzzolo, V. The Bio-Based Industries Joint Undertaking as a Catalyst for a Green Transition in Europe under the European Green Deal. *EFB Bioeconomy J.* **2021**, *1*, 100014.

(4) Lizundia, E.; Meaurio, E.; Vilas, J. L. Grafting of Cellulose Nanocrystals. *Multifunctional Polymeric Nanocomposites Based on Cellulosic Reinforcements*; Puglia, D., Fortunati, E., Kenny, J. M., Eds.; William Andrew: Norwich, NY, 2016; pp 61−113.

(5) Parton, T. G.; Parker, R. M.; van de Kerkhof, G. T.; Narkevicius, A.; Haataja, J. S.; Frka-Petesic, B.; Vignolini, S. Chiral Self-Assembly of Cellulose Nanocrystals Is Driven by Crystallite Bundles. *Nat. Commun.* **2022**, *13* (1), 2657.

(6) Kose, O.; Tran, A.; Lewis, L.; Hamad, W. Y.; MacLachlan, M. J. Unwinding a Spiral of Cellulose Nanocrystals for Stimuli-Responsive Stretchable Optics. *Nat. Commun.* **2019**, *10* (1), 510.

(7) Latif, M.; Jiang, Y.; Kumar, B.; Cho, H. C.; Song, J. M.; Kim, J. Three-Dimensional Printing of Highly Crosslinked and Concentrated Nanocellulose for Environmentally Friendly Structural Applications. *ACS Appl. Nano Mater.* **2022**, *5* (4), 5680−5687.

(8) Vorobiov, V. K.; Sokolova, M. P.; Bobrova, N. V.; Elokhovsky, V. Y.; Smirnov, M. A. Rheological Properties and 3D-Printability of Cellulose Nanocrystals/Deep Eutectic Solvent Electroactive Ion Gels. *Carbohydr. Polym.* **2022**, *290*, 119475.

(9) Imlimthan, S.; Correia, A.; Figueiredo, P.; Lintinen, K.; Balasubramanian, V.; Airaksinen, A. J.; Kostiainen, M. A.; Santos, H. A.; Sarparanta, M. Systematic in Vitro Biocompatibility Studies of Multimodal Cellulose Nanocrystal and Lignin Nanoparticles. *J. Biomed. Mater. Res., Part A* **2020**, *108* (3), 770−783.

(10) Mittal, N.; Ojanguren, A.; Cavasin, N.; Lizundia, E.; Niederberger, M. Transient Rechargeable Battery with a High Lithium Transport Number Cellulosic Separator. *Adv. Funct. Mater.* **2021**, *31* (33), 2101827.

(11) Lizundia, E.; Puglia, D.; Nguyen, T.-D.; Armentano, I. Cellulose Nanocrystal Based Multifunctional Nanohybrids. *Prog. Mater. Sci.* **2020**, *112*, 100668.

(12) Hausmann, M. K.; Rühs, P. A.; Siqueira, G.; Läuger, J.; Libanori, R.; Zimmermann, T.; Studart, A. R. Dynamics of Cellulose Nanocrystal Alignment during 3D Printing. *ACS Nano* **2018**, *12* (7), 6926−6937.

(13) Aeby, X.; Poulin, A.; Siqueira, G.; Hausmann, M. K.; Nyström, G. Fully 3D Printed and Disposable Paper Supercapacitors. *Adv. Mater.* **2021**, *33* (26), 2101328.

(14) Rincón-Iglesias, M.; Rodrigo, I.; Berganza, L. B.; Serea, E. S. A.; Plazaola, F.; Lanceros-Méndez, S.; Lizundia, E.; Reguera, J. Core-Shell Fe_3O_4@Au Nanorod-Loaded Gels for Tunable and Anisotropic Magneto- and Photothermia. *ACS Appl. Mater. Interfaces* **2022**, *14* (5), 7130−7140.

(15) Mahmoud, K. A.; Male, K. B.; Hrapovic, S.; Luong, J. H. T. Cellulose Nanocrystal/Gold Nanoparticle Composite as a Matrix for Enzyme Immobilization. *ACS Appl. Mater. Interfaces* **2009**, *1* (7), 1383−1386.

(16) Saeed, A. A.; Abbas, M. N.; Singh, B.; Abou-Zeid, R. E.; Kamel, S. Cellulose Nanocrystals Decorated with Gold Nanoparticles Immobilizing GO_x Enzyme for Non-Invasive Biosensing of Human Salivary Glucose. *Anal. Methods* **2019**, *11* (48), 6073−6083.

(17) Reguera, J.; Langer, J.; Jiménez de Aberasturi, D.; Liz-Marzán, L. M. Anisotropic Metal Nanoparticles for Surface Enhanced Raman Scattering. *Chem. Soc. Rev.* **2017**, *46* (13), 3866−3885.

(18) Ganguly, K.; Patel, D. K.; Dutta, S. D.; Lim, K.-T. TEMPO-Cellulose Nanocrystal-Capped Gold Nanoparticles for Colorimetric Detection of Pathogenic DNA. *ACS Omega* **2021**, *6* (19), 12424−12431.

(19) Majoinen, J.; Hassinen, J.; Haataja, J. S.; Rekola, H. T.; Kontturi, E.; Kostiainen, M. A.; Ras, R. H. A.; Törmä, P.; Ikkala, O. Chiral Plasmonics Using Twisting along Cellulose Nanocrystals as a Template for Gold Nanoparticles. *Adv. Mater.* **2016**, *28* (26), 5262−5267.

(20) Depciuch, J.; Stec, M.; Maximienko, A.; Baran, J.; Parlinska-Wojtan, M. Size-Dependent Theoretical and Experimental Photo-thermal Conversion Efficiency of Spherical Gold Nanoparticles. *Photodiagnosis Photodyn. Ther.* **2022**, *39*, 102979.

(21) Vines, J. B.; Yoon, J.-H.; Ryu, N.-E.; Lim, D.-J.; Park, H. Gold Nanoparticles for Photothermal Cancer Therapy. *Front. Chem.* **2019**, *7*, 167.

(22) Gharatape, A.; Davaran, S.; Salehi, R.; Hamishehkar, H. Engineered Gold Nanoparticles for Photothermal Cancer Therapy and Bacteria Killing. *RSC Adv.* **2016**, *6* (112), 111482−111516.

(23) Zhou, W.; Hu, K.; Kwee, S.; Tang, L.; Wang, Z.; Xia, J.; Li, X. Gold Nanoparticle Aggregation-Induced Quantitative Photothermal Biosensing Using a Thermometer: A Simple and Universal Biosensing Platform. *Anal. Chem.* **2020**, *92* (3), 2739−2747.

(24) Huang, X.; Tang, S.; Mu, X.; Dai, Y.; Chen, G.; Zhou, Z.; Ruan, F.; Yang, Z.; Zheng, N. Freestanding Palladium Nanosheets with Plasmonic and Catalytic Properties. *Nat. Nanotechnol.* **2011**, *6* (1), 28−32.

(25) Shen, S.; Wang, Q. Rational Tuning the Optical Properties of Metal Sulfide Nanocrystals and Their Applications. *Chem. Mater.* **2013**, *25* (8), 1166−1178.

(26) European Commission. Study on the Critical Raw Materials for the EU 2023 - Final Report. 2023. https://single-market-economy.ec.europa.eu/publications/study-critical-raw-materials-eu-2023-final-report_en (accessed on Oct, 2023).

(27) Grzelczak, M.; Vermant, J.; Furst, E. M.; Liz-Marzán, L. M. Directed Self-Assembly of Nanoparticles. *ACS Nano* **2010**, *4* (7), 3591−3605.

(28) Wang, C.; Song, F.; Wang, X.-L.; Wang, Y.-Z. A Cellulose Nanocrystal Templating Approach to Synthesize Size-Controlled Gold Nanoparticles with High Catalytic Activity. *Int. J. Biol. Macromol.* **2022**, *209*, 464−471.

(29) Lin, W.; Sun, W.; Yang, J.; Sun, Q.; Shen, Z. Fabrication of Magnetic Thin Films by a Layer-by-Layer Self-Assembly Approach. *J. Phys. Chem. C* **2009**, *113* (39), 16884−16895.

(30) Wan, Y.; Jiang, H.; Ren, Y.; Liu, Y.; Zhang, L.; Lei, Q.; Zhu, D.; Liu, J.; Zhang, X.; Ma, N.; Cong, X. Photothermal Self-Healable Polypyrrole-Polyurethane Sponge with Dynamic Covalent Oximino Bonds for Flexible Strain Sensors. *Eur. Polym. J.* **2023**, *193*, 112097.

(31) Nesser, H.; Grisolia, J.; Alnasser, T.; Viallet, B.; Ressier, L. Towards Wireless Highly Sensitive Capacitive Strain Sensors Based on Gold Colloidal Nanoparticles. *Nanoscale* **2018**, *10* (22), 10479−10487.

(32) Turkevich, J.; Stevenson, P. C.; Hillier, J. A Study of the Nucleation and Growth Processes in the Synthesis of Colloidal Gold. *Discuss. Faraday Soc.* **1951**, *11*, 55−75.

(33) Pallavicini, P.; Donà, A.; Taglietti, A.; Minzioni, P.; Patrini, M.; Dacarro, G.; Chirico, G.; Sironi, L.; Bloise, N.; Visai, L.; Scarabelli, L. Self-Assembled Monolayers of Gold Nanostars: A Convenient Tool for near-IR Photothermal Biofilm Eradication. *Chem. Commun.* **2014**, *50* (16), 1969−1971.

(34) Bastús, N. G.; Comenge, J.; Puntes, V. Kinetically Controlled Seeded Growth Synthesis of Citrate-Stabilized Gold Nanoparticles of up to 200 Nm: Size Focusing versus Ostwald Ripening. *Langmuir* **2011**, *27* (17), 11098−11105.

(35) Litti, L.; Reguera, J.; García de Abajo, F. J.; Meneghetti, M.; Liz-Marzán, L. M. Manipulating Chemistry through Nanoparticle Morphology. *Nanoscale Horiz.* **2020**, *5* (1), 102−108.

(36) Lizundia, E.; Goikuria, U.; Vilas, J. L.; Cristofaro, F.; Bruni, G.; Fortunati, E.; Armentano, I.; Visai, L.; Torre, L. Metal Nanoparticles Embedded in Cellulose Nanocrystal Based Films: Material Properties and Post-Use Analysis. *Biomacromolecules* **2018**, *19* (7), 2618−2628.

(37) Shukla, R.; Bansal, V.; Chaudhary, M.; Basu, A.; Bhonde, R. R.; Sastry, M. Biocompatibility of Gold Nanoparticles and Their Endocytotic Fate Inside the Cellular Compartment: A Microscopic Overview. *Langmuir* **2005**, *21* (23), 10644−10654.

(38) Mittal, N.; Ojanguren, A.; Niederberger, M.; Lizundia, E. Degradation Behavior, Biocompatibility, Electrochemical Performance, and Circularity Potential of Transient Batteries. *Adv. Sci.* **2021**, *8* (12), 2004814.

(39) Schumacher, M.; Jimenez de Aberasturi, D.; Merkl, J.-P.; Scarabelli, L.; Lenzi, E.; Henriksen-Lacey, M.; Liz-Marzán, L. M.; Weller, H. Robust Encapsulation of Biocompatible Gold Nanosphere Assemblies for Bioimaging via Surface Enhanced Raman Scattering. *Adv. Opt. Mater.* **2022**, *10* (14), 2102635.

(40) Kokol, V.; Pottathara, Y. B.; Mihelčič, M.; Perše, L. S. Rheological Properties of Gelatine Hydrogels Affected by Flow- and Horizontally-Induced Cooling Rates during 3D Cryo-Printing. *Colloids Surf., A* **2021**, *616*, 126356.

(41) Oliveira, J.; Correia, V.; Castro, H.; Martins, P.; Lanceros-Mendez, S. Polymer-Based Smart Materials by Printing Technologies: Improving Application and Integration. *Addit. Manuf.* **2018**, *21*, 269−283.

(42) Aeby, X.; Bourely, J.; Poulin, A.; Siqueira, G.; Nyström, G.; Briand, D. Printed Humidity Sensors from Renewable and Biodegradable Materials. *Adv. Mater. Technol.* **2023**, *8* (5), 2201302.

(43) Rincón-Iglesias, M.; Delgado, A.; Peřinka, N.; Lizundia, E.; Lanceros-Méndez, S. Water-Based 2D Printing of Magnetically Active Cellulose Derivative Nanocomposites. *Carbohydr. Polym.* **2020**, *233*, 115855.

(44) Conti, F.; Wiedemann, L.; Sonnleitner, M.; Goldbrunner, M. Thermal Behaviour of Viscosity of Aqueous Cellulose Solutions to Emulate Biomass in Anaerobic Digesters. *New J. Chem.* **2018**, *42* (2), 1099−1104.

(45) Eremeeva, E.; Sergeeva, E.; Neterebskaia, V.; Morozova, S.; Kolchanov, D.; Morozov, M.; Chernyshov, I.; Milichko, V.; Vinogradov, A. Printing of Colorful Cellulose Nanocrystalline Patterns Visible in Linearly Polarized Light. *ACS Appl. Mater. Interfaces* **2020**, *12* (40), 45145−45154.

(46) Kokol, V.; Vivod, V.; Peršin, Z.; Kamppuri, T.; Dobnik-Dubrovski, P. Screen-Printing of Microfibrillated Cellulose for an Improved Moisture Management, Strength and Abrasion Resistant Properties of Flame-Resistant Fabrics. *Cellulose* **2021**, *28* (10), 6663−6678.

(47) Baniasadi, H.; Kimiaei, E.; Polez, R. T.; Ajdary, R.; Rojas, O. J.; Österberg, M.; Seppälä, J. High-Resolution 3D Printing of Xanthan Gum/Nanocellulose Bio-Inks. *Int. J. Biol. Macromol.* **2022**, *209*, 2020−2031.

(48) Li, J.; Nawaz, H.; Wu, J.; Zhang, J.; Wan, J.; Mi, Q.; Yu, J.; Zhang, J. All-Cellulose Composites Based on the Self-Reinforced Effect. *Compos. Commun.* **2018**, *9*, 42−53.

(49) Alle, M.; Lee, S.-H.; Kim, J.-C. Ultrafast Synthesis of Gold Nanoparticles on Cellulose Nanocrystals via Microwave Irradiation and Their Dyes-Degradation Catalytic Activity. *J. Mater. Sci. Technol.* **2020**, *41*, 168−177.

(50) Shi, Z.; Tang, J.; Chen, L.; Yan, C.; Tanvir, S.; Anderson, W. A.; Berry, R. M.; Tam, K. C. Enhanced Colloidal Stability and Antibacterial Performance of Silver Nanoparticles/Cellulose Nanocrystal Hybrids. *J. Mater. Chem. B* **2015**, *3* (4), 603−611.

(51) Shaikh, H. M.; Anis, A.; Poulose, A. M.; Al-Zahrani, S. M.; Madhar, N. A.; Alhamidi, A.; Aldeligan, S. H.; Alsubaie, F. S. Synthesis and Characterization of Cellulose Triacetate Obtained from Date Palm (Phoenix Dactylifera L.) Trunk Mesh-Derived Cellulose. *Molecules* **2022**, *27* (4), 1434.

(52) Li, W.; Lin, C.; Ma, W.; Li, Y.; Chu, F.; Huang, B.; Yao, S. Transparent Selective Photothermal Coatings for Antifogging Applications. *Cell Rep. Phys. Sci.* **2021**, *2* (5), 100435.

(53) Leppänen, I.; Vikman, M.; Harlin, A.; Orelma, H. Enzymatic Degradation and Pilot-Scale Composting of Cellulose-Based Films with Different Chemical Structures. *J. Polym. Environ.* **2020**, *28* (2), 458−470.

(54) Cui, X.; Ruan, Q.; Zhuo, X.; Xia, X.; Hu, J.; Fu, R.; Li, Y.; Wang, J.; Xu, H. Photothermal Nanomaterials: A Powerful Light-to-Heat Converter. *Chem. Rev.* **2023**, *123* (11), 6891−6952.

(55) Roper, D. K.; Ahn, W.; Hoepfner, M. Microscale Heat Transfer Transduced by Surface Plasmon Resonant Gold Nanoparticles. *J. Phys. Chem. C* **2007**, *111* (9), 3636−3641.

(56) Lizundia, E.; Urruchi, A.; Vilas, J. L.; León, L. Increased Functional Properties and Thermal Stability of Flexible Cellulose Nanocrystal/ZnO Films. *Carbohydr. Polym.* **2016**, *136*, 250−258.

(57) Erdmann, R.; Kabasci, S.; Heim, H.-P. Thermal Properties of Plasticized Cellulose Acetate and Its β-Relaxation Phenomenon. *Polymers* **2021**, *13* (9), 1356.

(58) Uthaman, S.; Cutshaw, G.; Ghazvini, S.; Bardhan, R. Nanomaterials for Natural Killer Cell-Based Immunoimaging and Immunotherapies in Cancer. *ACS Appl. Mater. Interfaces* **2023**, *15* (44), 50708−50720.

(59) Wu, S.; Liang, Z.; Li, Y.; Chay, S.; He, Z.; Tan, S.; Wang, J.; Zhu, X.; He, X. Transparent, Photothermal, and Icephobic Surfaces via Layer-by-Layer Assembly. *Adv. Sci.* **2022**, *9* (14), 2105986.

(60) Mustakeem, M.; El-Demellawi, J. K.; Obaid, M.; Ming, F.; Alshareef, H. N.; Ghaffour, N. MXene-Coated Membranes for Autonomous Solar-Driven Desalination. *ACS Appl. Mater. Interfaces* **2022**, *14* (4), 5265−5274.

(61) Younis, M. R.; An, R. B.; Yin, Y.-C.; Wang, S.; Ye, D.; Xia, X.-H. Plasmonic Nanohybrid with High Photothermal Conversion Efficiency for Simultaneously Effective Antibacterial/Anticancer Photothermal Therapy. *ACS Appl. Bio Mater.* **2019**, *2* (9), 3942−3953.

(62) Freddi, S.; Sironi, L.; D'Antuono, R.; Morone, D.; Donà, A.; Cabrini, E.; D'Alfonso, L.; Collini, M.; Pallavicini, P.; Baldi, G.; Maggioni, D.; Chirico, G. A Molecular Thermometer for Nanoparticles for Optical Hyperthermia. *Nano Lett.* **2013**, *13* (5), 2004−2010.

(63) Mori, R. Replacing All Petroleum-Based Chemical Products with Natural Biomass-Based Chemical Products: A Tutorial Review. *RSC Sustainability* **2023**, *1* (2), 179−212.

(64) Saxena, S.; Johnson, M.; Dixit, F.; Zimmermann, K.; Chaudhuri, S.; Kaka, F.; Kandasubramanian, B. Thinking Green with 2-D and 3-D MXenes: Environment Friendly Synthesis and

Industrial Scale Applications and Global Impact. *Renew. Sustain. Energy Rev.* **2023**, *178*, 113238.

(65) Bundschuh, M.; Filser, J.; Lüderwald, S.; McKee, M. S.; Metreveli, G.; Schaumann, G. E.; Schulz, R.; Wagner, S. Nanoparticles in the Environment: Where Do We Come from, Where Do We Go To? *Environ. Sci. Eur.* **2018**, *30* (1), 6.

(66) Li, V. C. F.; Dunn, C. K.; Zhang, Z.; Deng, Y.; Qi, H. J. Direct Ink Write (DIW) 3D Printed Cellulose Nanocrystal Aerogel Structures. *Sci. Rep.* **2017**, *7* (1), 8018.

(67) Müller, L. A. E.; Zingg, A.; Arcifa, A.; Zimmermann, T.; Nyström, G.; Burgert, I.; Siqueira, G. Functionalized Cellulose Nanocrystals as Active Reinforcements for Light-Actuated 3D-Printed Structures. *ACS Nano* **2022**, *16* (11), 18210−18222.

(68) Molina-González, J.; Arellano-Morales, A.; Meza, O.; Ramírez-García, G.; Desirena, H. An Anti-Counterfeiting Strategy Based on Thermochromic Pigment Activated by Highly Yb^{3+} Doped Photo-thermal Particles. *J. Alloys Compd.* **2021**, *850*, 156709.

(69) Xu, C.; Huang, C.; Yang, D.; Luo, L.; Huang, S. Photo-Luminescent Photonic Crystals for Anti-Counterfeiting. *ACS Omega* **2022**, *7* (8), 7320−7326.

(70) Song, C.; Wang, Z.; Yin, Z.; Xiao, D.; Ma, D. Principles and Applications of Photothermal Catalysis. *Chem Catal.* **2022**, *2* (1), 52−83.